

Too few spots in the Cosmic Microwave Background

Youness Ayaita, Maik Weber, Christof Wetterich

*Institut für Theoretische Physik, Universität Heidelberg
Philosophenweg 16, D-69120 Heidelberg, Germany*

We investigate the abundance of large-scale hot and cold spots in the WMAP-5 temperature maps and find considerable discrepancies compared to Gaussian simulations based on the Λ CDM best-fit model. Too few spots are present in the reliably observed CMB region, i.e. outside the foreground-contaminated parts excluded by the KQ75 mask. This can only partially be explained by the well-known quadrupole anomaly. Even simulated maps created from the original WMAP-5 estimated multipoles contain more spots than visible in the measured CMB maps. We analyze two possible origins of the discrepancies: statistical anisotropy violating Gaussianity (spots are distributed differently outside and inside the masked region) or an even more drastic lack of power than implied by the low quadrupole. This lack of power on scales of several degrees, quantified by the mean temperature fluctuation, is only shared by less than 1% of Gaussian Λ CDM simulations. We show that the discrepancies disappear when the lowest multipoles are strongly suppressed.

I. INTRODUCTION

The precise measurement of anisotropies in the Cosmic Microwave Background (CMB) has played a key role in amplifying our knowledge about the structure and evolution of the universe. The best data available today is provided by the Wilkinson Microwave Anisotropy Probe (WMAP) satellite mission from five years of observation (Limon et al., 2008). Its results are powerful enough to put various cosmological models to stringent tests. They helped establishing today's standard model of a spatially flat universe with Gaussian initial perturbations, possibly generated during an early inflationary epoch. According to the standard Λ CDM model, the present universe is essentially made up from dark energy in the form of a cosmological constant Λ and cold dark matter (CDM). Under the assumption of Gaussianity, all the information about the temperature fluctuations in the CMB are encoded in the angular power spectrum C_l from a harmonic decomposition of the temperature field. A crucial result of the WMAP analysis therefore is an estimate of the multipoles C_l which is in good agreement with the Λ CDM best fit (Nolta et al., 2009) except for the well-known discrepancies of the low multipoles, especially the quadrupole C_2 (Hinshaw et al., 2007). Nonetheless, many issues are still under intense discussion. Repeatedly, authors have claimed to detect non-Gaussian signals (McEwen et al., 2008; Yadav and Wandelt, 2008) or in particular statistical anisotropy (Bernui et al., 2006; de Oliveira-Costa et al., 2004; Eriksen et al., 2004; Hansen et al., 2008; Hoftuft et al., 2009; Land and Magueijo, 2005). Since the power spectrum is insensitive to these anomalies, it is necessary to perform additional investigations of the temperature sky map. These are done in harmonic, wavelet and pixel space (Cabella et al., 2004). Even if Gaussianity holds, it may still give new insights to switch to another representation of the statistical properties of the temperature maps since a phenomenon can be more easily detected in one representation than in another.

The goal of this work is to provide a clear and intuitive analysis in pixel space regarding abundances of large-scale hot and cold spots identified as regions whose mean temperature contrasts exceed some (variable) threshold. We

analyze both observed CMB maps and Gaussian simulations based on Λ CDM. The comparison reveals more severe deviations than expected from the quadrupole anomaly. Other authors who worked with statistics of local extrema in the temperature field also observed significant anomalies (Hou et al., 2009; Larson and Wandelt, 2004, 2005).

We start by recalling some basic results that connect pixel-space analyses with the angular power spectrum in section II. A comprehensive description of our method follows in section III including the preparation of adequate Gaussian simulations, the working principle of our spot searching algorithm and an error estimation. Our results are presented in section IV. We consider both cut-sky maps (with unreliable pixels excluded by the KQ75 temperature analysis mask) and the Internal Linear Combination (ILC) full-sky map, and quantify deviations from Gaussian simulations. We sum up and conclude in section V.

II. PRELIMINARY CONSIDERATIONS

The most robust comparison between predicted and observed spot abundances of CMB sky maps relies on simulated maps since analytic methods can hardly care for complications due to masking and beam properties. Creating a number of simulated maps and treating them in exactly the same way as the original map therefore is the clearest method. Nonetheless, it is instructive to recall some well-known analytic results that connect the pixel-space analysis to familiar harmonic space.

The spot abundances in a CMB sky map are dictated by the angular correlations of temperature fluctuations. The most popular theories stick to Gaussianity which in particular implies statistical isotropy. Then, the ensemble average of the angular correlation between two directions (θ, φ) and (θ', φ') only depends on the angle Θ between them. This leads to the definition of the angular correlation function

$$C(\Theta) = \left\langle \frac{\Delta T}{T}(\theta, \varphi) \times \frac{\Delta T}{T}(\theta', \varphi') \right\rangle. \quad (1)$$

We can switch to harmonic space by decomposing the tem-

perature field into spherical harmonics:

$$\frac{\Delta T}{\bar{T}}(\theta, \varphi) = \sum_{l,m} a_{lm} Y_{lm}(\theta, \varphi). \quad (2)$$

where the crucial assumption of statistical isotropy implies

$$\langle a_{lm} a_{l'm'}^* \rangle = \delta_{ll'} \delta_{mm'} C_l. \quad (3)$$

So, in this case, all the statistical information is in the coefficients C_l , the angular power spectrum. More generally, we may define

$$C_l = \frac{1}{2l+1} \sum_m \langle |a_{lm}|^2 \rangle. \quad (4)$$

When searching for spots of a given size, we will average the temperature fluctuations in regions of that size. These regions are defined by window functions $W(\theta, \varphi)$. The mean temperature contrast in such a region is

$$\Delta T = \int d\Omega \Delta T(\theta, \varphi) W(\theta, \varphi). \quad (5)$$

In our sense, a *spot* is characterized as follows. When a threshold $\Delta \mathfrak{T}$ is fixed, a *hot spot* is found if $\Delta T \geq \Delta \mathfrak{T}$, whereas a *cold spot* is found if $\Delta T \leq -\Delta \mathfrak{T}$. The characteristic scale for ΔT is the mean temperature contrast for these regions $\Delta T_{rms} = \sqrt{\langle \Delta T^2 \rangle}$. Clearly, if $\Delta \mathfrak{T} \ll \Delta T_{rms}$, most regions will be spots, if $\Delta \mathfrak{T} \gg \Delta T_{rms}$, only a few or none.

The transformation to harmonic space can be done by decomposing the window function $W(\theta, \varphi)$ into spherical harmonics with coefficients W_{lm} and defining

$$W_l = \sum_m |W_{lm}|^2. \quad (6)$$

Together with equations (2) and (3), it is straightforward to calculate

$$\Delta T_{rms}^2 = \sum_l \frac{2l+1}{4\pi} C_l W_l \bar{T}^2. \quad (7)$$

This result shows that the mean temperature fluctuation ΔT_{rms} is given by the multipoles C_l weighted by W_l . The W_l strongly depend on the angular scale of the regions. Their magnitude will suppress large l values corresponding to scales smaller than the window. By virtue of the addition theorem for spherical harmonics, we can write

$$W_l = \int d\Omega \int d\Omega' W(\theta, \varphi) W(\theta', \varphi') P_l(\cos \Theta). \quad (8)$$

This allows us to calculate the W_l for a chosen window. An example is shown in figure 1.

In our case, it is adequate to approximate the sphere by the tangent plane at a region, replacing the direction (θ, φ) by points \mathbf{x} on the plane. For our purposes, it is most convenient to work with top hat windows because they have clear boundaries. This is the easiest way to avoid ambiguities arising from overlapping spots. Exemplary choices may be the top hat circle with window function

$$W(\mathbf{x}) = \frac{1}{\pi R^2} \Theta(R - |\mathbf{x}|) \quad (9)$$

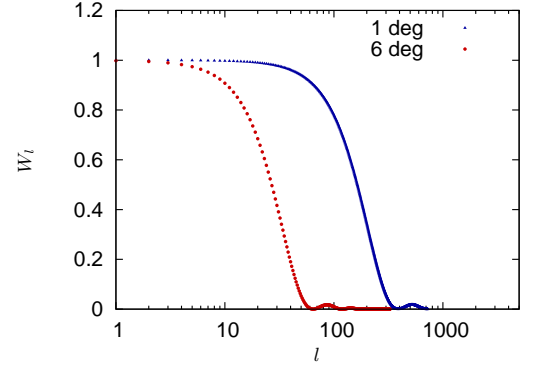


FIG. 1 Coefficients W_l for the top hat circle window function at scales $a = 1^\circ$ (right plot), 6° (left plot). The plots show which C_l predominantly determine ΔT_{rms} . For smaller angular scale a , higher l values enter the analysis.

or a square with window function

$$W(\mathbf{x}) = \frac{1}{a^2} \Theta(a - x_1) \Theta(a - x_2). \quad (10)$$

Following Durrer (2008, p. 218), we can approximate the W_l by an angular average over the Fourier transform of $W(\mathbf{x})$ which considerably reduces the computational effort:

$$W_l \approx \frac{1}{2\pi} \int_0^{2\pi} d\alpha |\tilde{W}(\mathbf{l})|^2. \quad (11)$$

For the aforementioned window functions, we can use this equation to easily calculate ΔT_{rms} by equation (7). The results are plotted for the Λ CDM best fit power spectrum in figure 2. For the sake of comparability, we use the parameter a which equals the square root of the windows' area; in the case of squares, it simply is the side length. We also show the relative deviation due to the different window functions. We conclude that the result is not sensitive to the exact geometry if the covered surface area is the same.

III. METHOD

Our strategy consists of performing an identical analysis of spot abundances both for observational maps and maps generated from simulations of Gaussian fluctuations. For the simulated maps, we use the best-fit Λ CDM model and a Gaussian fluctuation model based on the C_l quoted by the WMAP collaboration. The comparison with maps from observation tests Gaussianity and the assumed power spectrum.

Due to the excellent data products of the WMAP team (Limon et al., 2008) available at the legacy archive¹ and the comprehensive HEALPix package² (Górski et al.,

¹ <http://cmbdata.gsfc.nasa.gov>

² <http://healpix.jpl.nasa.gov>

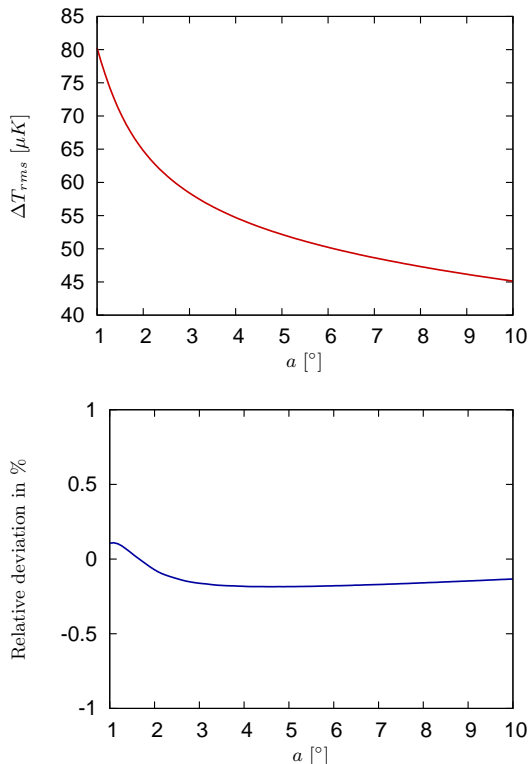


FIG. 2 Mean temperature fluctuation for various spot sizes and the Λ CDM power spectrum. The plots for circles and squares are visually indistinguishable. The difference between the result for circles and the result for squares is shown in the second figure.

2005), it is possible to obtain reliable CMB sky maps and to create maps from Gaussian simulations. We summarize the steps in section III.A. We developed an algorithm searching for hot and cold spots (in the sense of section II) within these temperature sky maps. Its working principle and properties are presented in section III.B. The treatment of statistical errors is described in section III.C.

A. Maps and data preparation

Whenever the original signal is to be extracted from CMB data, it is crucial to minimize the influence of foreground contamination. The frequency dependence of the foreground components (e.g. synchrotron emission, free-free emission and thermal dust) allows to reduce the contamination with the help of various foreground models (Gold et al., 2009). The WMAP team provides foreground-reduced maps for the Q (35-46 GHz), V (53-69 GHz) and W (82-106 GHz) bands. Since the V band has a better signal-to-noise ratio than the W band and is less foreground contaminated than the Q band (Hinshaw et al., 2007), it is the natural choice to use the foreground-reduced V-band map. Further noise minimization by constructing linear combinations of the maps is possible but does not affect our analysis which focuses on large scales. But still, large parts of the temperature map are unreliable and must

be excluded from the analysis. We therefore apply the KQ75 mask cutting out the contaminated galaxy region and point sources (Gold et al., 2009). Finally, the residual monopole and dipole are removed with the HEALPix routine REMOVE_DIPOLE. Figure 3 shows the foreground-reduced V-band map and the KQ75 mask.

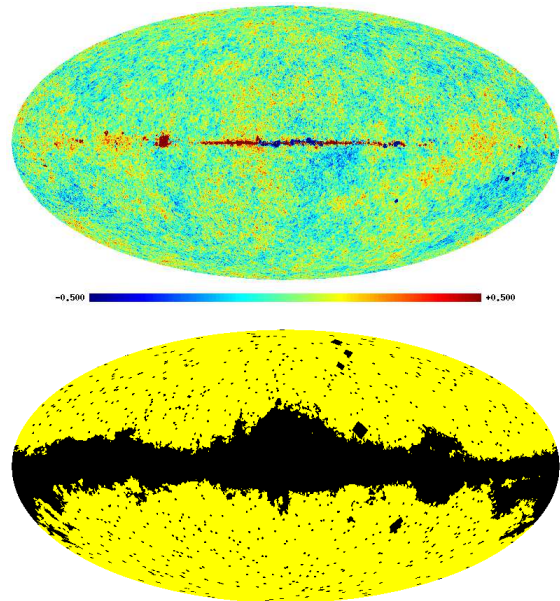


FIG. 3 The foreground-reduced V-band map (temperature contrast in mK) and the KQ75 mask cutting out the contaminated galaxy region and point sources.

Gaussian simulations based on some input C_l spectrum and a beam window function are achieved with the help of the SYNFAST HEALPix facility. These input data can be obtained from the legacy archive. The power spectra we used are the Λ CDM best fit and the original WMAP-5 estimate both shown in figure 1 of Nolte et al. (2009). Subsequently, we will refer to them by “ Λ CDM” and “WMAP-5” power spectrum for short. We take care of treating simulated and original maps as equally as possible. This necessitates the additional simulation of the instruments’ noise, masking and removal of monopole and dipole. Since the WMAP design minimizes noise correlation between neighboring pixels in a map (Page et al., 2003), it is legitimate to add white noise with the properties described by the WMAP team (Limon et al., 2008, p. 54).

When studying possible anisotropy of the CMB, we need a full-sky (unmasked) map. Since the foreground contaminations usually force us to mask parts of the sky, it is not a trivial task to reconstruct the full-sky CMB signal. However, the WMAP team tries to tackle this job by combining the measurements of all bands and merge them into a single (ILC) map of the full sky (Gold et al., 2009). The applied procedure is independent of foreground models but has the disadvantage of being doubtful on scales below approximately 10° according to the WMAP product description (Limon et al., 2008, p. 82). But since we are lacking any better alternative, we employ the 5-year WMAP ILC map for full-sky analyses.

B. Spot searching algorithm

The primary goal of the algorithm is to count hot and cold spots in CMB sky maps on various scales and temperature contrasts. A typical application will be to plot spot abundances against the threshold on the temperature contrast $\Delta\mathfrak{T}$ for a specific angular scale. This application directly imposes several features the algorithm should have:

- (i) It must define *sectors on the sphere of equal surface area* (for some desired scale). Their mean temperature contrasts will decide whether they are counted as spots.
- (ii) The areas must be chosen such that one can *smoothly scan* through the map. Between two distinct areas, there must exist many others allowing for a smooth transition.
- (iii) Double counting of spots has to be excluded. The easiest way to achieve this is working with *top hat windows* which have clear boundaries. Overlapping spots will be counted as a single.
- (iv) For a statistically satisfactory comparison between observed and simulated CMB maps, the algorithm will have to analyze many sky maps. Given the huge amount of data, one has to implement the algorithm carefully in order to make this *numerically tractable*.

The algorithm is designed such that it allows for an approximate pixelization of the sphere into distinct areas of a given scale. Calculating their temperature contrasts determines the mean temperature fluctuation ΔT_{rms} on that scale. By virtue of the ergodic theorem, this is a good estimate for the ensemble average introduced in section II.

1. Working principle

The first task is to define the sectors S of equal surface area on the sphere satisfying the requirements explained above. We choose them to be intersections of latitude and longitude rings. A latitude ring \mathcal{R}^{lat} consists of all points between two latitude angles θ_0 and θ_1 , a longitude ring \mathcal{R}^{lon} of all points between two longitude angles φ_0 and φ_1 . The rings have two nice properties. Firstly, as needed for spot searching, one can smoothly go from one ring to any other ring by smoothly changing its boundary angles; secondly, as needed for calculating ΔT_{rms} , it is an easy task to discretize a sphere into distinct rings. Since sectors are intersections $S = \mathcal{R}^{lat} \cap \mathcal{R}^{lon}$, they share these properties. We thereby satisfy the requirement of smooth scanning to all directions. Once we have decided to define sectors like this, we have still some freedom to choose the boundaries $\theta_0, \theta_1, \varphi_0, \varphi_1$. In order to avoid the influence of small scales, we must reasonably choose the sectors such that they are by no means degenerated. We therefore fix this freedom by adding another constraint. For any sector S , the boundary lines in the north-south direction and the longer boundary in the east-west direction must be of equal length. Together with the condition of equal area,

the algorithm will choose sectors such that:

$$\int_{\varphi_0}^{\varphi_1} d\varphi \int_{\theta_0}^{\theta_1} d\theta \sin \theta = A \quad (12)$$

$$(\varphi_1 - \varphi_0) \sin \theta_* = (\theta_1 - \theta_0) \quad (13)$$

On the northern hemisphere $\theta_* = \theta_1$, on the southern hemisphere $\theta_* = \theta_0$. Note that these sectors behave well. In the limiting case near the equator, they correspond to squares in flat space. At the poles ($\theta_0 = 0$ or $\theta_1 = \pi$), they become equilateral triangles. A visualization of the sectors is shown in figure 4.

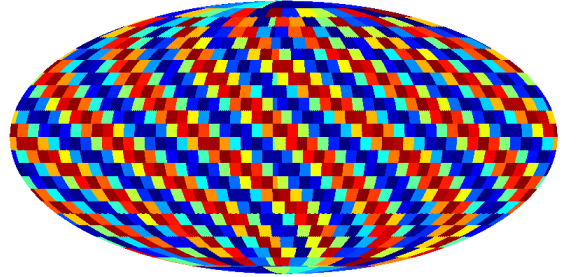


FIG. 4 Exemplary decomposition of the sky into sectors defined by the algorithm.

In practice though, the temperature field is not given as a smooth function of θ and φ . The WMAP temperature sky maps are lists assigning a temperature contrast ΔT_i to each HEALPix pixel p_i . The mapping $p_i \mapsto (\theta, \varphi)$ is given in the form of a table. But since our approach defines sectors by means of angles, we need the reverse. Given the list $p_i \mapsto (\theta, \varphi)$, finding the appropriate pixel p_i for given angles (θ, φ) corresponds to searching through the list. Whereas searching in an unsorted list is very expensive, an adequate sorting may considerably reduce the effort. The algorithm performs the following steps starting at the north pole $\theta_0 = 0$:

1. For given θ_0 and area A , calculate θ_1 and $\Delta\varphi$ by solving equations (12) and (13).
2. Collect the pixels $\{p_i\}$ belonging to the latitude ring \mathcal{R}^{lat} between θ_0 and θ_1 . This can be done efficiently if the map was prepared by transforming to sorted latitude angles (HEALPix RING ordering).
3. Using a fast routine, sort the list $\{p_i\}$ with respect to longitude angles. This new sorting allows one to directly identify the pixels out of $\{p_i\}$ belonging to a longitude ring \mathcal{R}^{lon} with boundaries φ_0 and φ_1 —these pixels form the sector $S = \mathcal{R}^{lat} \cap \mathcal{R}^{lon}$. Start at $\varphi_0 = 0$ and $\varphi_1 = \Delta\varphi$ and smoothly scan through all longitude rings. For every sector, calculate the sector's mean temperature contrast ΔT by averaging over the pixel values ΔT_i and compare it with the threshold $\Delta\mathfrak{T}$. If it exceeds the threshold, count a spot if the sector doesn't overlap with a previously found spot.
4. Choose the next ring by slightly increasing θ_0 . It is profitable to exploit the fact that the sorting for

longitude angles (point 3) needn't be repeated completely. The algorithm saves the previous sorting and uses it for a pre-sort such that as much information is transferred as possible.

Having increased the threshold $\Delta\mathfrak{T}$, again searching for spot abundances in a map can be optimized by noticing that spots at a higher threshold cannot be found where there weren't spots at a lower threshold. Our algorithm can focus on areas around previously found spots once this becomes advantageous.

If we slightly adapt the algorithm, we can use it to measure ΔT_{rms} . Now, the algorithm jumps between distinct sectors instead of smoothly transforming them. In every distinct sector, the mean temperature fluctuation is calculated. The squares are averaged to give ΔT_{rms} . Although the shapes of the sectors vary, the results of section II ensure that ΔT_{rms} is only marginally affected.

2. Treatment of masked maps

The sectors defined by our algorithm may include none, some or many masked pixels. We must define selection rules determining which sectors are to be included in the statistics. We used the following two rules. The most restrictive choice is to only consider sectors with no mask overlap (*strict selection* for short). These sectors will only contain reliable pixels. But since especially on large scales, only a minority of sectors will belong to this group, bad statistics are the price to pay. The alternative choice is to also consider sectors with a slight mask overlap (*tolerant selection*). This is a compromise between good statistics on the one hand and reliable results on the other. We typically allow for 5% masked area within a sector which guarantees that usually the majority of sectors fall into this group. In any case, we emphasize that masked pixels, even if included in the statistics, are assigned zero temperature fluctuation. This will avoid misinterpreting foregrounds as a CMB signal. Note however, that the pixels of zero temperature fluctuation reduce ΔT_{rms} . For comparisons between observed maps and Gaussian simulations, we employ the tolerant selection for the sake of better statistics; the comparison is still trustworthy.

3. Alternative shapes

The algorithm works with the shapes defined in section III.B.1 and illustrated in figure 4. But we can easily treat other shapes by embedding them into the previous sectors. This corresponds to a multiplication of the previous window function W_0 with the window function W_1 of the desired shape where W_0 must be large enough to ensure $W_0 \equiv 1$ where W_1 is non-zero. The condition (12) of equal area now concerns the new shape and reads

$$\int_{\varphi_0}^{\varphi_1} d\varphi \int_{\theta_0}^{\theta_1} d\theta \sin \theta W_1(\theta, \varphi) = A. \quad (14)$$

As an example, we compare the standard shape with top hat circles of equal area (cf. eq. 9) and plot the result in

figure 5. For low thresholds, the abundances are system-

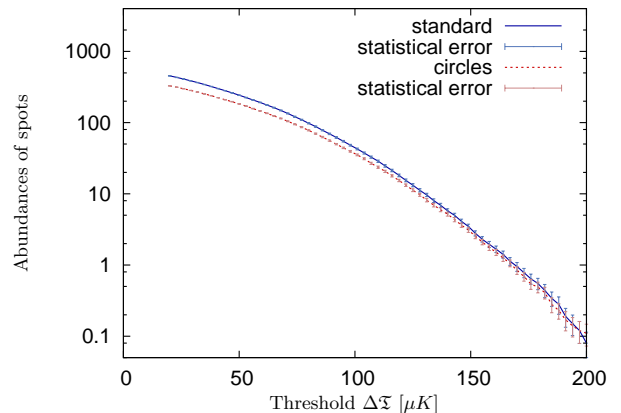


FIG. 5 Mean spot abundances in 100 simulated Λ CDM full-sky maps showing the results for different window functions of scale $a = \sqrt{A} = 6^\circ$.

atically higher for the standard window function. This is due to the fact that circles do not exhaust the area without space in between. The effect becomes important where many spots are found and overlapping is frequent but disappears for large thresholds where the results agree.

4. Step size dependence

In the ideal case, the boundary angles of the sectors would vary in a perfectly smooth manner when searching for spots in a map. But numerically, we have to choose a finite step size h . A good choice of h balances sensitivity and numerical effort. Figure 6 shows detected spot abundances against h in simulated maps. We chose $h = 0.3^\circ$ for which we conclude that our sensitivity to detect spots is satisfactory.

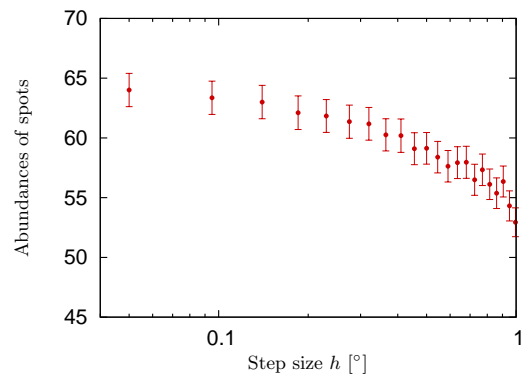


FIG. 6 Mean spot abundances for a fixed threshold ($80 \mu K$) against a varying step size. 100 masked Λ CDM simulated maps were scanned for $a = 6^\circ$, the error bars quantify the statistical error.

C. Errors and cosmic variance

A crucial requirement for drawing conclusions is an adequate estimation of errors. There are statistical uncertainties simply due to the finite number of Gaussian simulations. Moreover, the CMB signal itself can be regarded as the outcome of a statistical process. It is therefore subject to statistical variation, quantified by the concept of cosmic variance.

Let us assume that N Gaussian maps are analyzed for spots (area and threshold fixed). If $n^{(k)}$ spots are detected in map k , the mean spot abundance is

$$\bar{n} = \sum_{k=1}^N \frac{n^{(k)}}{N}. \quad (15)$$

The statistical uncertainty of the mean value \bar{n} and the statistical deviation of the single values $\bar{n}^{(k)}$ are

$$\sigma_{\bar{n}}^2 = \frac{\sum_{k=1}^N (n^{(k)} - \bar{n})^2}{N(N-1)}, \quad \sigma_{n^{(k)}}^2 = N \sigma_{\bar{n}}^2. \quad (16)$$

The same procedure applies if we measure the mean temperature fluctuations $\Delta T_{rms}^{(k)}$ in the maps and calculate a mean value $\Delta \bar{T}_{rms}^{(k)}$.

We now consider cosmic variance. When we observe a spot abundance n , we must expect a certain deviation from the theoretically predicted ensemble average $\langle n \rangle$. The expectation value of this deviation, $\sigma_n^2 = \langle n - \langle n \rangle \rangle^2$, quantifies cosmic variance. For a very large number N of simulated maps, we may replace the ensemble average by an averaging over the set of simulations. We then obtain $\sigma_n \approx \sigma_{n^{(k)}}$ with the latter calculated according to equation (16). This can be done equally for the mean temperature contrast ΔT_{rms} . Whenever we specify cosmic variance (e.g. in the form of error bars), we estimated it by this method.

IV. RESULTS

The application of the spot-searching algorithm described in section III shows that the standard model Λ CDM together with Gaussianity predicts more large-scale hot and cold spots than are actually present in cut-sky WMAP-5 data (see section IV.A). Using the original WMAP-5 C_l instead of the Λ CDM fit reduces the discrepancies but does not settle the issue. We discuss possible sources which lead to an investigation of full-sky maps in section IV.B and of modifications of the first multipoles in section IV.C.

A. Cut-sky maps

The spots' size is characterized by their area A . We use the parameter $a = \sqrt{A}$ to specify the angular scale of this size. Since on the one hand, we aim at large scales, and on the other hand, we want reasonable statistics, we are forced to find a compromise. We chose an angular scale $a = 6^\circ$. The spot abundances of the WMAP-5 V-band map and 500 Gaussian Λ CDM simulations (created as described in section III.A) are found for varying threshold

$\Delta \mathfrak{T}$. The HEALPix resolution parameter of the maps is 8, corresponding to $N_{pix} = 12 \times 256^2 = 786,432$ pixels. Statistical uncertainties and cosmic variance are displayed as error bars even though the spot abundances for different thresholds are of course correlated. The results for hot and cold spots are plotted in figure 7. The striking feature

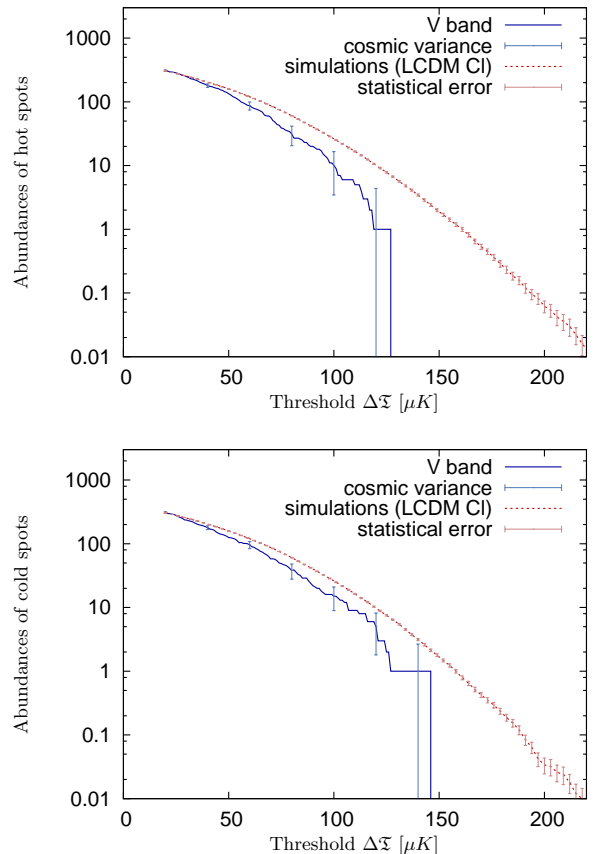


FIG. 7 Spot abundances in the CMB sky as compared to 500 Λ CDM simulations on an angular scale of $a = 6^\circ$.

of the plots is the systematic discrepancy between theory and observation. They only agree in the limit of very small thresholds $\Delta \mathfrak{T}$ where it is obvious that anyway almost every area is counted as a spot. The discrepancy is seemingly more drastic for hot spots. In the plot for cold spots, it is seen that there is one considerable cold spot nearly reaching $150 \mu K$. But even this spot does not surpass the Λ CDM prediction. We note that this spot is localized in the region of the famous Vielva Cold Spot (Vielva et al., 2004).

The discrepancies are reflected in the mean temperature fluctuation ΔT_{rms} which on large scales is higher in Λ CDM simulations than in the observed CMB sky. We have simulated 5000 Λ CDM maps and compared their mean temperature fluctuations to the value of the V-band map. We employed the tolerant selection of our algorithm (see section III.B.2). For $a = 6^\circ$, we find the mean value $\Delta T_{rms} = 39.4 \mu K$ for the V-band map, as compared to the mean value $\Delta \bar{T}_{rms} = 47.9 \pm 0.1 \mu K$ for Λ CDM, where the error is only statistical while cosmic variance amounts to $4.2 \mu K$. Only a fraction $p = 0.6\%$ of the simulations had

TABLE I The fraction p of Gaussian Λ CDM simulations with a ΔT_{rms} smaller than found in the V map on the angular scale a .

Scale a	Fraction p
4°	0.50%
5°	0.62%
6°	0.60%
7°	0.16%
8°	0.36%

a smaller ΔT_{rms} than the V map. This does not improve at other large angular scales which can be seen in table I. It is interesting to see how this behavior changes when going to smaller scales. However, the results on smaller scales (approaching 1°) become sensitive to noise and beam properties. Since the WMAP team offers the latter for the differencing assemblies V1 and V2 (Hill et al., 2009) instead of the combined V map, it is the easiest to switch to the V1-band map and simulations thereof. The impact on large scales is negligible. Figure 8 shows ΔT_{rms} against the scale a for the V1 map and Λ CDM simulations (again with tolerant selection). We see that the deviations decrease when

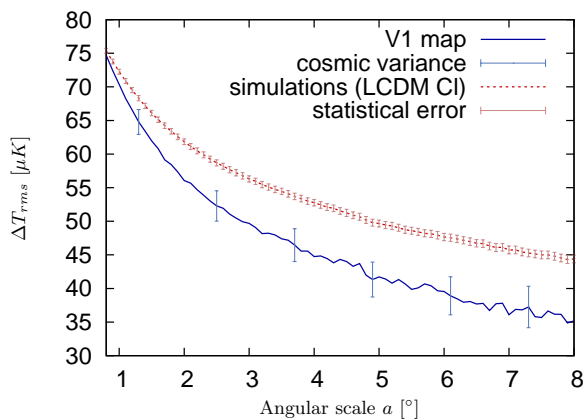


FIG. 8 The mean temperature fluctuation for different angular scales a in fifty Gaussian Λ CDM simulations and the V1 map.

going to smaller scales. This is also suggested by the C_l spectrum which is in good agreement with the Λ CDM fit for large l which dominate on small scales.

For this analysis, we used the highest available HEALPix resolution 9 corresponding to $N_{pix} = 12 \times 512^2 = 3,145,728$ pixels in a map. As stated above, the plots are highly influenced by the beam function and noise. The beam function acts as an extra window function which suppresses the growth of ΔT_{rms} for small scales. The white noise instead leads to a diverging $1/a$ behavior on the smallest scales (with an effective pixel noise amplitude σ_{pix} and the number of pixels $N_a = N_{pix} \times a^2/4\pi$ within a sector of scale a , the noise contribution will be $\Delta T_{rms}^{noise} = \sigma_{pix}/\sqrt{N_a} \propto 1/a$).

On large scales, the first multipoles of the C_l spectrum play an important role (see e.g. figure 1). It is there-

fore a natural idea to suspect the well-known quadrupole anomaly (Hinshaw et al., 2007) to be responsible for the observed discrepancies. We check this by repeating the analysis for Gaussian simulations based on the original WMAP-5 C_l spectrum which has a much lower quadrupole C_2 than the Λ CDM best fit. Figure 9 shows the spot abundances. The effect arising from changing the power

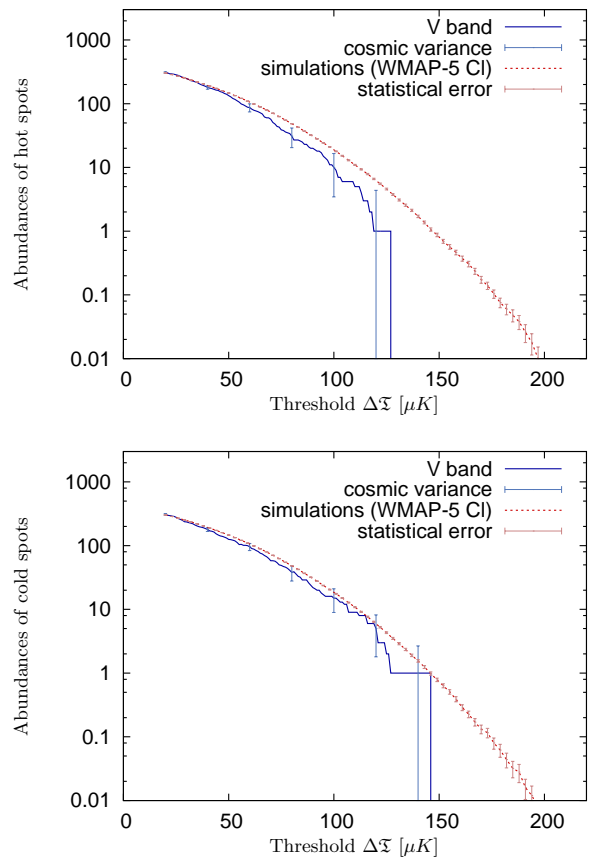


FIG. 9 Spot abundances in the CMB sky as compared to 500 simulations based on the WMAP-5 C_l spectrum on an angular scale of $a = 6^\circ$.

spectrum is clearly visible and reduces the discrepancies to some extent. But although closer to the spot abundances in the observed cut-sky CMB map, the numbers of hot and cold spots are still systematically too high. Again, this is reflected in the fact that most simulated maps have a larger ΔT_{rms} than the V map. Even though the values, listed in table II, are less drastic, we emphasize that the WMAP-5 estimation of the C_l relies on similar data, i.e. cut-sky CMB maps.

Bearing in mind that power spectra refer to the full sky whereas we only look at regions outside the mask, all this could still be consistent if the missing spots were located in the hidden part of the sky. In the next section, we investigate whether the WMAP-5 ILC map indicates this violation of isotropy.

TABLE II The fraction p of 1000 Gaussian simulations (WMAP-5 C_l) with a ΔT_{rms} smaller than found in the V map on the angular scale a .

Scale a	Fraction p
4°	4.2%
5°	5.4%
6°	5.8%
7°	2.4%
8°	4.1%

B. ILC full-sky map

The five-year ILC map is the best approximate full-sky CMB map available. We therefore analyze it even though the quality of the reconstruction is not high enough to guarantee robustness of the results (see also section III.A). We analyze the ILC full-sky map and 100 Gaussian full-sky simulations based on the WMAP-5 power spectrum and separately consider the results in three sky regions. Firstly, we analyze the full sky. Secondly, we collect the spots of those regions that have also been studied in the V-band map, i.e. regions with no or little overlap with the KQ75 mask (tolerant selection). Finally, we consider the remaining spots that consequently lie in sectors completely inside the mask or with considerable mask overlap (rejected by tolerant selection). We loosely refer to the three regions as *full sky*, *outside* and *inside mask*. The results are plotted in figure 10. In the previously analyzed region (outside the mask), we see systematically too few spots, as before. But there are by far too many spots in the complementary region. The ILC map is clearly anisotropic. Other authors draw the same conclusion (Bernui and Reboucas, 2009; Copi et al., 2008; Hajian, 2007).

Anisotropy of the CMB is a possible explanation of the discrepancies revealed in section IV.A and quantified in table I, and indeed, the ILC map contains this anisotropy. But since there is not enough reliable information about the CMB signal in the galactic plane, we cannot finally judge whether this is the true solution to the problem. We have also studied if, additionally to the galactic plane, the orientation of the galactic halo defines a preferred direction. Therefore, we divided the ILC map into two halves, one around the galactic center and one covering the opposite direction. We have seen no signal of anisotropy in this direction.

C. Modified power spectra

We have seen that anisotropy is a potential explanation. It is however unsatisfying to assume that so many additional spots lie in the contaminated regions hidden by the KQ75 mask. This would be a surprising coincidence of CMB signals and the orientation of the galactic plane. In addition, statistical anisotropy in particular implies a violation of Gaussianity. It is thus important to wonder whether there are suitable solutions within the realm of Gaussian-

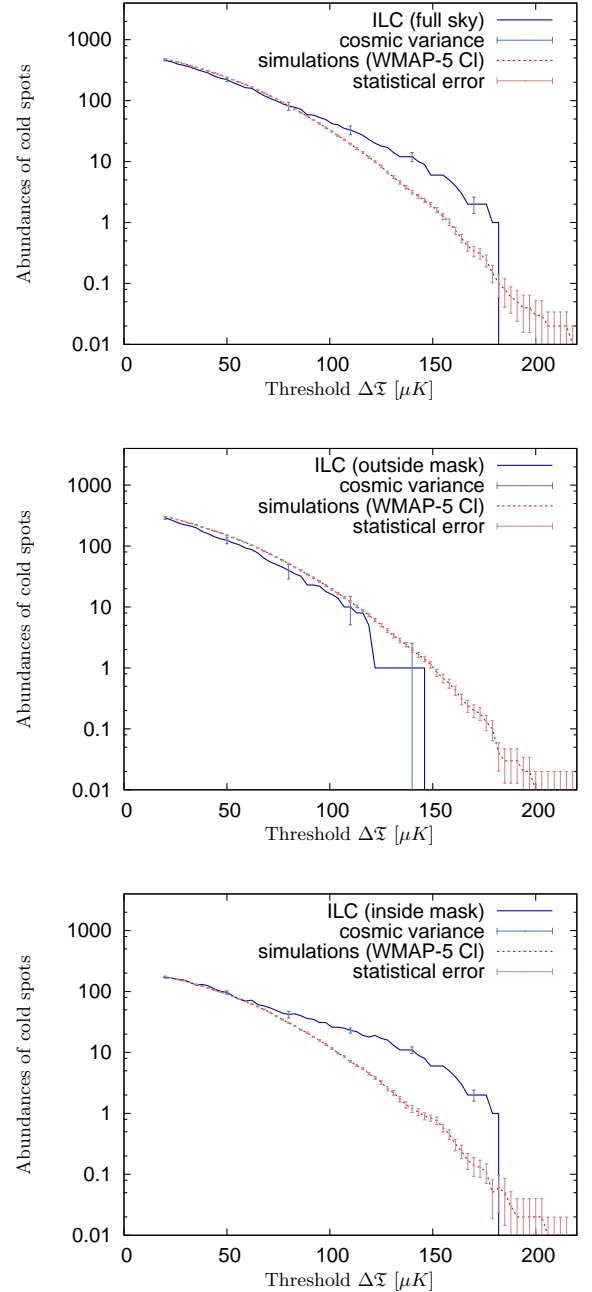


FIG. 10 Spot abundances in the ILC map compared with simulations based on the measured WMAP-5 C_l on an angular scale of $a = 6^\circ$ for three different parts of the sky.

ity. So far, ΔT_{rms} has proved to be a good parameter to quantify the visible effects. But all values of ΔT_{rms} could of course be explained without giving up Gaussianity if the C_l are modified (cf. eq. 7). We can perform a quick check whether our data so far supports the hypothesis that ΔT_{rms} is the decisive parameter. Out of the 500 simulations with the WMAP-5 power spectrum used in section IV.A, we collect those with a ΔT_{rms} smaller or equal than found in the V map. Figure 11 shows their spot abundances which agree well with the V map.

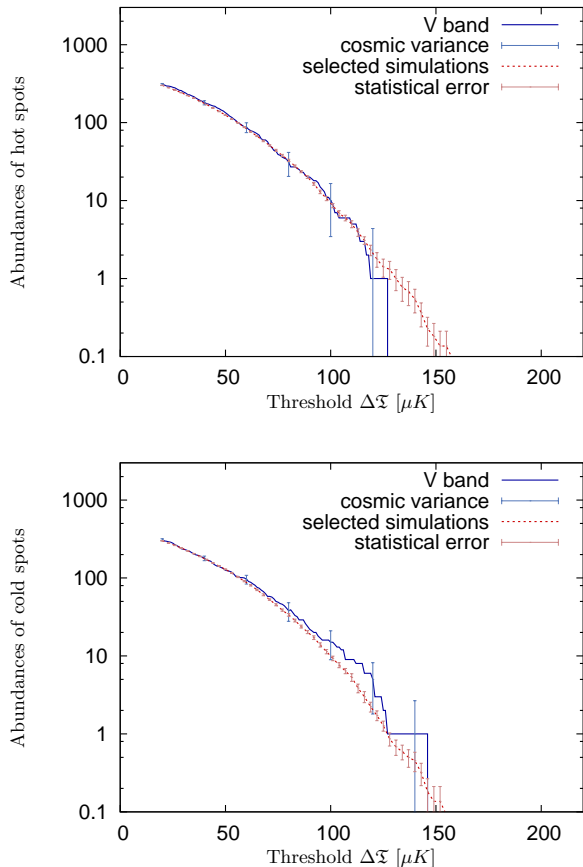


FIG. 11 Spot abundances of Gaussian simulations k with $\Delta T_{rms}^{(k)} \leq \Delta T_{rms}^{V \text{ map}}$.

We are therefore naturally driven to the idea of finding modified C_l spectra that produce a ΔT_{rms} similar to the one found in the V map. In order to keep the analysis as generic as possible, we do not use any specific cosmological model but only modify the C_l of the original WMAP-5 spectrum. Figure 8 suggests that only large scales are affected which is why we concentrate on a few low multipoles l . Copi et al. (2008) found that the correlation function is essentially zero on angular scales above $\approx 60^\circ$. Since this scale is roughly linked to the multipole range $l \leq 3$, our first modification simply consists in setting $C_l \equiv 0$ for $l \leq 3$ (although of course the correlation function does not translate this easily). Another example may be to halve the C_l for $l \leq 5$ (modification II). Figure 12 shows the resulting values of ΔT_{rms} . The plots show the discrepancies between the Λ CDM prediction, the WMAP-5 spectrum and observation. We also show the results for a combined power spectrum, replacing the first 32 multipoles by the values quoted by WMAP-1 (Hinshaw et al., 2003). For this range of multipoles the WMAP analysis changed after the 1-year release, following the suggestion of Efstathiou (2004). The difference between WMAP-5 and WMAP-1 may serve as an illustration that the extraction of reliable C_l for low l is a non-trivial task. The modifications I and II of the power spectrum succeeded in reconciling Gaussian simula-

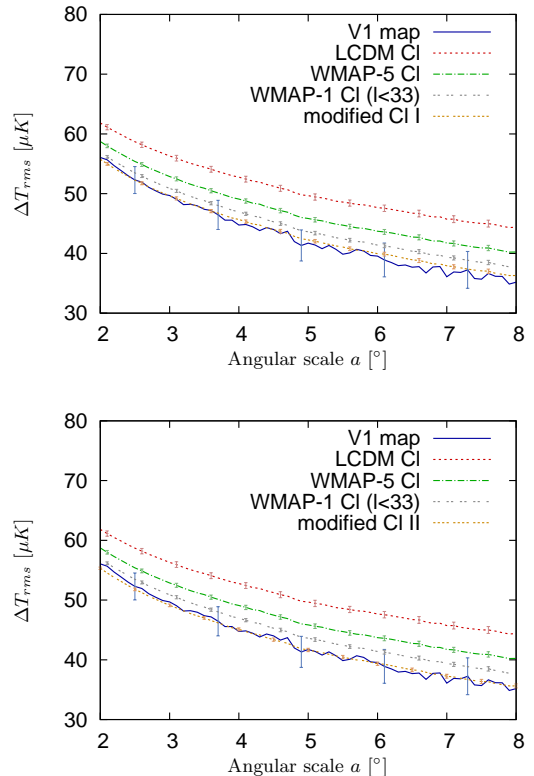


FIG. 12 The mean temperature fluctuation for large angular scales a . We compare the V1 map with Λ CDM simulations (highest ΔT_{rms}), simulations based on the WMAP-5 C_l (a bit lower), the WMAP-1 C_l for $l < 33$ (still lower) and on two modified spectra. The first modification is created by setting $C_l = 0$ for $l \leq 3$, the second by halving the C_l for $l \leq 5$. The modified spectra agree well with the V1 map.

tions and observed CMB sky. This is confirmed by measuring the spot abundances in simulated maps based on the modified spectra, seen in figure 13. We conclude that our results are not incompatible with Gaussianity. However, if we stick to Gaussianity, they favor even lower values of the first multipoles than currently estimated.

V. CONCLUSIONS

The study of spot abundances has revealed discrepancies between the cut-sky CMB temperature maps and the standard best-fit Λ CDM model or a Gaussian spectrum for the C_l estimated by WMAP-5. We have shown in section IV.C that a good parameter to quantify them is the mean temperature fluctuation ΔT_{rms} which we investigated on large scales. On scales a between 4° and 8° , only 0.16% to 0.62% of Gaussian simulations based on the Λ CDM best-fit power spectrum fall below the ΔT_{rms} value of the observed V-band CMB map. If this merely was an imprint of the anomalously low quadrupole, we would have expected the discrepancies to disappear when exchanging the Λ CDM best-fit spectrum by the originally published WMAP-5 C_l . Though the difference reduces a bit, we still

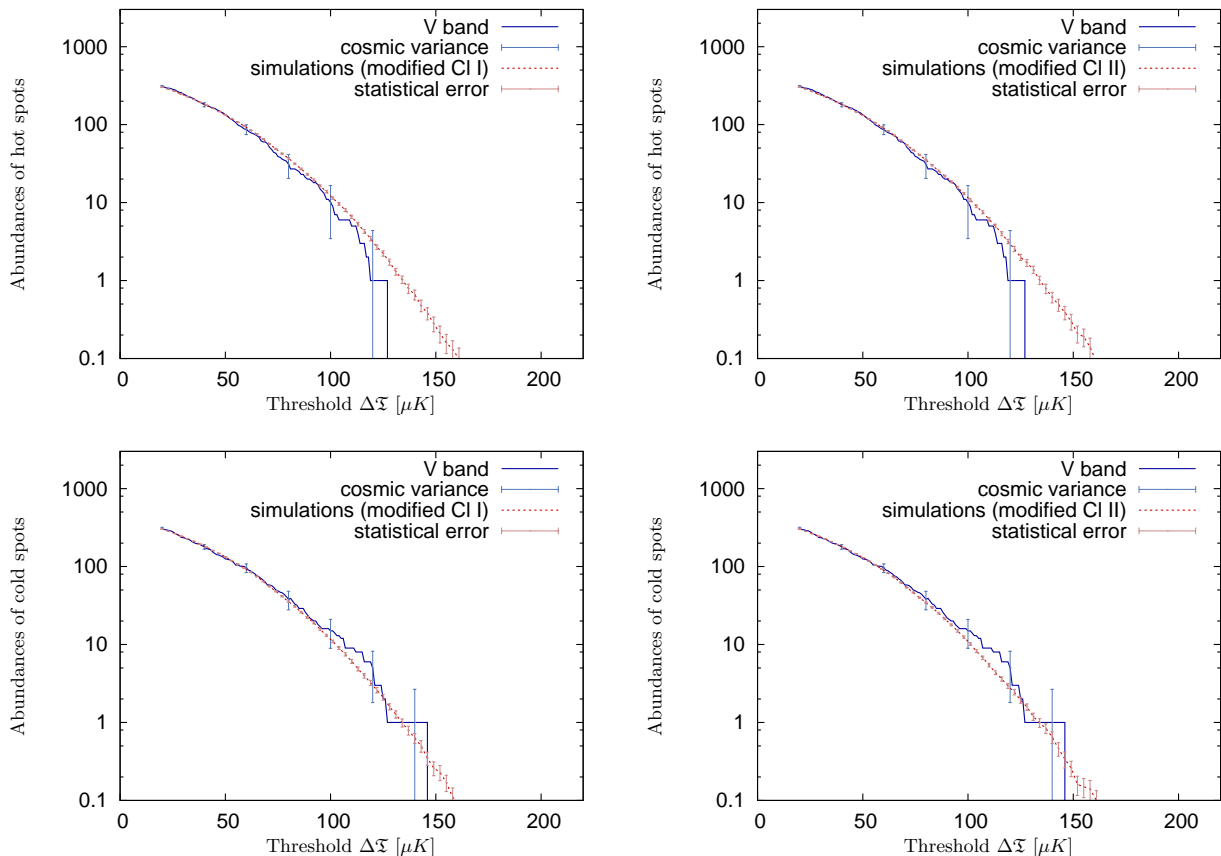


FIG. 13 Spot abundances in the CMB sky as compared to 100 simulations based on the two modified spectra respectively on an angular scale of $a = 6^\circ$.

do not find agreement between the observed map and simulations. The aforementioned fractions change to 2.4% to 5.8%. This is difficult to understand if we bear in mind that the C_l themselves are estimated from the cut-sky CMB maps (Nolta et al., 2009).

If we give up the fundamental assumption of Gaussianity, statistical anisotropy is a possible explanation. In our case, this means that many spots have to be hidden behind the masked region. Unfortunately, this hypothesis can hardly be tested as there is currently no method to reliably extract the CMB signal in the highly foreground-contaminated regions. Nonetheless, we have employed the WMAP-5 ILC full-sky CMB map and found evidence for anisotropy in this map. This agrees with results obtained by Hajian (2007) and Copi et al. (2008) who found that most of the power on the largest scales comes from the (masked) galaxy region. Though possible, this unnatural alignment of the CMB signal with the galactic plane would be intriguing and lacks so far any explanation.

We have also studied the alternative approach of retaining Gaussianity. Our analysis of section IV.C shows that our results for cut-sky maps do not suggest non-Gaussianity by themselves. They are compatible with Gaussian fluctuations if one performs a modification of the lowest multipoles. In doing so, no fine-tuning of the C_l is necessary in order to reconcile the spot abundances from

Gaussian simulations and the observed CMB. It is sufficient to lower the first multipoles by a substantial amount. When studying local extrema in the temperature field, Hou et al. (2009) similarly found discrepancies that disappeared when excluding the first multipoles. We recall, however, that the C_l and the assumption of Gaussianity completely fix the expected spot abundances. If both the extraction of the C_l by WMAP-5 and our analysis of spot abundances are correct, the assumption of a Gaussian spectrum cannot be maintained.

If the discrepancies are not caused by mere statistical coincidence or unknown secondary effects, we have to leave open the question whether we see the consequence of anisotropy or whether the lack of large-scale power is more severe than commonly thought. The first case would violate Gaussianity, the second would make it difficult to understand the CMB maps on large scales within standard Λ CDM cosmology. If the discrepancies between the C_l , as determined by WMAP-5, and the spot abundances persist, this can be interpreted as a signal for non-Gaussian fluctuations.

Acknowledgements

We would like to thank Christian T. Byrnes for useful discussions. We also thank the WMAP team for producing great data products (Limon et al., 2008) and publishing them on LAMBDA (the Legacy Archive for Microwave Background Data Analysis). Support for LAMBDA is provided by the NASA Office of Space Science. We acknowledge the use of the HEALPix package (Górski et al., 2005) that we employed for many tasks, most notably the creation and preparation of Gaussian simulations.

References

- Bernui, A. and Reboucas, M. J. (2009). Searching for non-Gaussianity in the WMAP data. *Phys. Rev.*, D79:063528, arXiv:0806.3758.
- Bernui, A., Villela, T., Wuensche, C. A., Leonardi, R., and Ferreira, I. (2006). On the CMB large-scales angular correlations. *Astron. Astrophys.*, 454:409–414, arXiv:astro-ph/0601593.
- Cabella, P., Hansen, F., Marinucci, D., Pagano, D., and Vittorio, N. (2004). Search for non-Gaussianity in pixel, harmonic and wavelet space: compared and combined. *Phys. Rev.*, D69:063007, arXiv:astro-ph/0401307.
- Copi, C. J., Huterer, D., Schwarz, D. J., and Starkman, G. D. (2008). No large-angle correlations on the non-Galactic microwave sky. arXiv:0808.3767.
- de Oliveira-Costa, A., Tegmark, M., Zaldarriaga, M., and Hamilton, A. (2004). The significance of the largest scale CMB fluctuations in WMAP. *Phys. Rev.*, D69:063516, arXiv:astro-ph/0307282.
- Durrer, R. (2008). *The Cosmic Microwave Background*. Cambridge University Press.
- Efstathiou, G. (2004). A Maximum Likelihood Analysis of the Low CMB Multipoles from WMAP. *Mon. Not. Roy. Astron. Soc.*, 348:885, arXiv:astro-ph/0310207.
- Eriksen, H. K., Hansen, F. K., Banday, A. J., Gorski, K. M., and Lilje, P. B. (2004). Asymmetries in the CMB anisotropy field. *Astrophys. J.*, 605:14–20, arXiv:astro-ph/0307507.
- Gold, B., Bennett, C. L., Hill, R. S., Hinshaw, G., Odegard, N., Spergel, D. N., Weiland, J., Dunkley, J., Halpern, M., Jarosik, N., Kogut, A., Komatsu, E., Larson, D., Meyer, S. S., Nolte, M., Wollack, E., and Wright, E. L. (2009). Five-Year Wilkinson Microwave Anisotropy Probe (WMAP) Observations: Galactic Foreground Emission. *ApJS*, 180:265–282, arXiv:0803.0715.
- Górski, K. M., Hivon, E., Banday, A., Wandelt, B., Hansen, F., Reinecke, M., and Bartelmann, M. (2005). HEALPix: A Framework for High-resolution Discretization and Fast Analysis of Data Distributed on the Sphere. *ApJ*, 622:759–771, arXiv:astro-ph/0409513.
- Hajian, A. (2007). Analysis of the apparent lack of power in the cosmic microwave background anisotropy at large angular scales. arXiv:astro-ph/0702723.
- Hansen, F. K., Banday, A. J., Gorski, K. M., Eriksen, H. K., and Lilje, P. B. (2008). Power Asymmetry in Cosmic Microwave Background Fluctuations from Full Sky to Sub-degree Scales: Is the Universe Isotropic? arXiv:0812.3795.
- Hill, R. S., Weiland, J. L., Odegard, N., Wollack, E., Hinshaw, G., Larson, D., Bennett, C. L., Halpern, M., Page, L., Dunkley, J., Gold, B., Jarosik, N., Kogut, A., Limon, M., Nolte, M., Spergel, D. N., Tucker, G. S., and Wright, E. L. (2009). Five-Year Wilkinson Microwave Anisotropy Probe (WMAP) Observations: Beam Maps and Window Functions. *ApJS*, 180:246–264, arXiv:0803.0570.
- Hinshaw, G., Nolte, M. R., Bennett, C. L., Bean, R., Doré, O., Greason, M. R., Halpern, M., Hill, R. S., Jarosik, N., Kogut, A., Komatsu, E., Limon, M., Odegard, N., Meyer, S. S., Page, L., Peiris, H. V., Spergel, D. N., Tucker, G. S., Verde, L., Weiland, J. L., Wollack, E., and Wright, E. L. (2007). Three-Year Wilkinson Microwave Anisotropy Probe (WMAP) Observations: Temperature Analysis. *ApJS*, 170:288–334, arXiv:astro-ph/0603451.
- Hinshaw, G., Spergel, D. N., Verde, L., Hill, R. S., Meyer, S. S., Barnes, C., Bennett, C. L., Halpern, M., Jarosik, N., Kogut, A., Komatsu, E., Limon, M., Page, L., Tucker, G. S., Weiland, J. L., Wollack, E., and Wright, E. L. (2003). First-Year Wilkinson Microwave Anisotropy Probe (WMAP) Observations: The Angular Power Spectrum. *ApJS*, 148:135–159, arXiv:astro-ph/0302217.
- Hoftuft, J., Eriksen, H. K., Banday, A. J., Górski, K. M., Hansen, F. K., and Lilje, P. (2009). Increasing evidence for hemispherical power asymmetry in the five-year WMAP data. arXiv:0903.1229.
- Hou, Z., Banday, A. J., and Gorski, K. M. (2009). The Hot and Cold Spots in Five-Year WMAP Data. arXiv:0903.4446.
- Land, K. and Magueijo, J. (2005). The axis of evil. *Phys. Rev. Lett.*, 95:071301, arXiv:astro-ph/0502237.
- Larson, D. L. and Wandelt, B. D. (2004). The Hot and Cold Spots in the WMAP Data are Not Hot and Cold Enough. *ApJ*, 613:L85–L88, arXiv:astro-ph/0404037.
- Larson, D. L. and Wandelt, B. D. (2005). A Statistically Robust 3-Sigma Detection of Non-Gaussianity in the WMAP Data Using Hot and Cold Spots. arXiv:astro-ph/0505046.
- Limon, M., Wollack, E., Greason, M. R., Bennett, C. L., Halpern, M., Hinshaw, G., Jarosik, N., Kogut, A., Meyer, S. S., Page, L., Spergel, D. N., Tucker, G. S., Wright, E. L., Hill, R. S., Komatsu, E., Nolte, M., Odegard, N., and Weiland, J. L. (2008). Wilkinson Microwave Anisotropy Probe (WMAP): Five Year Explanatory Supplement.
- McEwen, J. D., Hobson, M. P., Lasenby, A. N., and Mortlock, D. J. (2008). A high-significance detection of non-Gaussianity in the WMAP 5-year data using directional spherical wavelets. arXiv:0803.2157.
- Nolte, M. R., Dunkley, J., Hill, R. S., Hinshaw, G., Komatsu, E., Larson, D., Page, L., Spergel, D. N., Bennett, C. L., Gold, B., Jarosik, N., Odegard, N., Weiland, J. L., Wollack, E., Halpern, M., Kogut, A., Limon, M., Meyer, S. S., Tucker, G. S., and Wright, E. (2009). Five-Year Wilkinson Microwave Anisotropy Probe (WMAP) Observations: Angular Power Spectra. *ApJS*, 180:296–305, arXiv:0803.0593.
- Page, L., Jackson, C., Barnes, C., Bennett, C., Halpern, M., Hinshaw, G., Jarosik, N., Kogut, A., Limon, M., Meyer, S. S., Spergel, D. N., Tucker, G. S., Wilkinson, D. T., Wollack, E., and Wright, E. L. (2003). The Optical Design and Characterization of the Microwave Anisotropy Probe. *ApJ*, 585:566–586, arXiv:astro-ph/0301160.
- Vielva, P., Martínez-González, E., Barreiro, R. B., Sanz, J. L., and Cayón, L. (2004). Detection of non-Gaussianity in the WMAP 1-year data using spherical wavelets. *ApJ*, 609:22–34, arXiv:astro-ph/0310273.
- Yadav, A. P. S. and Wandelt, B. D. (2008). Evidence of Primordial Non-Gaussianity (f_{NL}) in the Wilkinson Microwave Anisotropy Probe 3-Year Data at 2.8σ . *Phys. Rev. Lett.*, 100:181301, arXiv:0712.1148.